



Published in final edited form as:

Med Image Anal. 2017 December ; 42: 173–188. doi:10.1016/j.media.2017.06.011.

Accurate Model-based Segmentation of Gynecologic Brachytherapy Catheter Collections in MRI-images

Andre Mastmeyer^{a,*}, Guillaume Pernelle^b, Rubin Ma^c, Lauren Barber^d, and Tina Kapur^{c,d,**}

^aInstitute of Medical Informatics, University of Luebeck, Germany

^bDepartment of Bioengineering, Imperial College London, United Kingdom

^cDepartment of Radiology, Brigham and Women's Hospital, Boston, MA, United States

^dHarvard Medical School, Boston, MA, United States

Abstract

The gynecological cancer mortality rate, including cervical, ovarian, vaginal and vulvar cancers, is more than 20,000 annually in the US alone. In many countries, including the US, external-beam radiotherapy followed by high dose rate brachytherapy is the standard-of-care. The superior ability of MR to visualize soft tissue has led to an increase in its usage in planning and delivering brachytherapy treatment. A technical challenge associated with the use of MRI imaging for brachytherapy, in contrast to that of CT imaging, is the visualization of catheters that are used to place radiation sources into cancerous tissue. We describe here a precise, accurate method for achieving catheter segmentation and visualization. The algorithm, with the assistance of manually provided tip locations, performs segmentation using image-features, and is guided by a catheter-specific, estimated mechanical model. A final quality control step removes outliers or conflicting catheter trajectories. The mean Hausdorff error on a 54 patient, 760 catheter reference database was 1.49 mm; 51 of the outliers deviated more than two catheter widths (3.4 mm) from the gold standard, corresponding to catheter identification accuracy of 93% in a Syed-Neblett template. In a multi-user simulation experiment for evaluating RMS precision by simulating varying manually-provided superior tip positions, 3σ maximum errors were 2.44 mm. The average segmentation time for a single catheter was 3 seconds on a standard PC. The segmentation time, accuracy and precision, are promising indicators of the value of this method for clinical translation of MR-guidance in gynecologic brachytherapy and other catheter-based interventional procedures.

Keywords

MRI; segmentation; catheter; outlier reduction; accuracy; precision

Corresponding author: Tina Kapur, PhD, Department of Radiology, Brigham and Women's Hospital, Harvard Medical School, 75 Francis Street, Boston, MA 02115, USA. Tel: (617) 732-5893, tkapur@bwh.harvard.edu.

*mastmeyer@imi.uni-luebeck.de

**tkapur@bwh.harvard.edu

1. Introduction

Gynecological malignancies, including those of the cervix, endometrium, ovaries, and external female genitalia, are a leading cause of mortality in women worldwide. In the United States, with an estimated 105,890 new cases and a mortality of 29%, gynecological malignancies continue to present a medical challenge (American Cancer Society, 2015). Chemoradiation, which consists of concurrent chemotherapy and external-beam radiation, followed by brachytherapy (Fig. 1) remains the standard-of-care for treatment of gynecologic cancers. Compared to external-beam radiation, brachytherapy allows for a higher total dose of radiation to a smaller area in less time, as the radiation sources are placed in direct contact with the cancerous tissue typically under CT- or X-ray-guidance (Han and Viswanathan, 2016). In high-dose-rate (HDR) interstitial brachytherapy, interstitial applicators with catheters that are approximately 20 cm long and 2 mm in diameter are inserted percutaneously through a standardized template surgically sutured to the patient's perineum (Fig. 2). The catheters are used as channels for bringing radiation seeds in close proximity to the targeted tissue and delivering high-dose radiation to the cancer.

In a survey by the American Brachytherapy Society, the utilization of MRI increased from 2% to 34% between 2007 and 2014 (Grover et al., 2016). This is not surprising, given the ability of MRI to provide better imaging of the tumor and adjacent soft tissues (compared to CT), and hence its routine use in the radiologic diagnosis of pelvic cancers (Jolesz, 2014). However, the artifacts created in MRI scans using typical brachytherapy catheters are considerably more difficult to interpret compared to CT (See Fig. 1a and 1b for CT imaging catheter artifacts, and Fig. 1c for MRI imaging catheter artifacts). Artifacts created by catheters used in pelvic brachytherapy are very distinct in X-ray or CT images and therefore, amenable to automatic segmentation using the standard image-processing techniques of commercial brachytherapy treatment planning products^{1,2}. This observation is primarily because voxels on these catheters correspond to a narrow range of high Hounsfield values that are distinct from human tissue in CT images. In contrast, the grayscale range of catheters in MRI scans overlaps with that of human tissue, and one part of the catheter can appear to be substantially different from another part of the same catheter while being difficult to distinguish from surrounding tissue (Rafat Zand et al., 2007). Today, there are no automatic solutions for the segmentation of brachytherapy catheters from MRI images (Song et al., 2012; DiMaio et al., 2005). Even manual segmentations from MRI are time-consuming, tedious, and error-prone because of the large numbers and high density of catheters in the images, and not used in clinical research or practice today.

We contribute to the state of research in the following ways:

1. **An innovative, customized algorithm:** Use of a mechanical catheter bending model to constrain an image-coupled segmentation process; an automatic error-correction step to analyze intersecting catheters and automatically correct the results.

¹Elekta, Stockholm, Sweden

²Varian Medical Systems, CA, USA

2. **A novel application area with a large database for medical image-analysis:** Accuracy and precision of the proposed method are illustrated on a database of 760 catheters in 54 patients including difficult cases with up to 40 catheters for MRI-guided high dose rate gynecologic brachytherapy, a novel and growing clinical application area. This is the first report using this database.
3. **Performance accuracy and precision improvement using stronger model assumptions.** We used a mechanical model to augment the Bezier-model (Pernelle et al., 2013).
4. **Precision evaluation:** A multiple user input simulation to estimate precision; also the first of its kind for MRI-guided high dose rate gynecological brachytherapy.

In summary, we present here a novel catheter segmentation method, with promising accuracy and precision numbers, that has been validated using a large MRI database containing hundreds of catheters.

2. State of the Art

Clinical Procedures: To the best of our knowledge, we are the first and only group to attempt segmentation of brachytherapy catheters from MRI images. The most plausible reason for this is that the use of MRI as a modality for planning and guiding the placement of high dose rate (HDR) gynecologic brachytherapy catheters, is a relatively recent development that was pioneered at our institution, Brigham and Women's Hospital (BWH), Boston (Jolesz, 2014; Damato and Viswanathan, 2015). Between 2012 and 2016, nearly a hundred such procedures were performed in a 3-Tesla MR scanner in the Advanced Multimodality Image-Guided Operating (AMIGO) suite at BWH which was built with support from the National Institutes of Health with the purpose of advancing the usage of appropriate imaging to guide therapy (Tempany et al., 2015). More recently, a clinical trial has been launched at Johns Hopkins University to further investigate the impact of MRI in assessing the tumor at the time of brachytherapy MRI and in reducing the radiation dose received by the body during the process of treating the tumor (Viswanathan, Akila N, 2016).

Elongated Structure Segmentation: There is a significant body of medical image computing literature on the segmentation of elongated, tubular, or curvilinear structures. The vast majority of reported methods target highly tortuous and branched structures such as white matter tracts in diffusion MRI images (Hao et al., 2014; O'Donnell and Westin, 2007), blood vessels in angiographic images (Kerrien et al., 2017; Lesage et al., 2016; Schneider et al., 2015; Manniesing et al., 2010; Schaap et al., 2007; Wink et al., 2004; Aylward and Bullitt, 2002), or nerves in MRI images (Sultana et al., 2017). Compared to e.g. Bayesian tracking of elongated structures proposed in (Schaap et al., 2007), we are using strong mechanical bending constraints while tracking. Some of the various tracking methods surveyed here are much more flexible, may account for bifurcations and thus would probably go astray by allowing much more and catheter-atypical curvature changes than we do. Some methods focus on segmentation of interventional hardware such as guidewires in angiographic images, which are also tortuous because they are inserted into blood vessels

(Vandini et al., 2017; Honnorat, 2013; Honnorat et al., 2010), and other methods focus on segmentation of less flexible intervention hardware such as biopsy needles in ultrasound images (Hrinivich et al., 2017; Pourtaherian et al., 2016; Daoud et al., 2015; Qiu et al., 2013; Aboofazeli et al., 2009; Okazawa et al., 2006; Czerwinski et al., 1999). Compelling results for segmentation of elongated structures – blood vessels and surgical hardware-using artificial neural networks have also been recently reported³, including for the segmentation of vessels from retinal images (Fu et al., 2016) and segmentation of surgical instruments from endoscopic images (Pakhomov et al., 2017).

We investigated two foundational ideas that have been applied in several of the articles mentioned above. In early work, we explored the vesselness metric (Frangi et al., 1998) which combines appearance and shape using Eigenvectors of local Hessian matrices, to enhance the tubular structure, but were unable to capture catheters with any level of success. It is possible that this was because the vesselness metric has been used most frequently in angiographic images where there is significant contrast between vessels and tissue. The contrast between catheters and tissue is not sharp in the T2-MRI scans of our application. More recently, we explored the use of Hough transform (Duda and Hart, 1972), a voting method which is used to find parametric shapes in an image. We implemented a 3D Hough transform and were able to detect up to two of the straightest and most prominent catheters in our images. Noise in the parameter space caused many false positive "catheters" (line segments) to be detected in the image space (oversegmentation), which is why we believe that this method could not scale up to the tens of catheters in our images.

Our Previous Work: In 2013, we reported our first results in the literature for the segmentation of brachytherapy catheters from MRI (Pernelle et al., 2013). In this work, each catheter is represented as a Bezier curve, and the control points of each curve are automatically detected using a raycasting-based search for a specific gray-level pattern in a series of cones. Starting from a user click t_0 ($i = 0$) on the superior catheter tip, the method searched for the best dark-line candidate inside conic volumes of radius r_{cone} towards the base of the cone (Fig. 3 illustrates one search cone). The objective function integrated the visited voxels in the image along the current ray. Mathematically, the method seeks superior to inferior line integrals that minimize the image intensity value $I(x)$, thus minimizing the line integral sum.

The optimal point c_{img} is computed as:

$$c_{img} = \underset{c_{img}}{\operatorname{argmin}} \left(\int_{t_i}^{c_{img}} I(x) dx \right) \quad (1)$$

and the resulting optimal line segment is $\vec{l}_{img} = \overrightarrow{t_i c_{img}}$ (Fig. 3). The process is then repeated using the accepted point c_{img} as tip, t_{i+1} for the next segment. A Bezier curve with N control points is used to combine these accepted points – from the tip t_0 and successive c_{img} from N

³see (Litjens et al., 2017) for a survey on deep learning based neural network methods for medical image analysis

– 1 search cones with increasing heights determined by a Fibonacci heuristic – into a trajectory for the catheter.

This method resulted in almost 90% identification accuracy in a database of 101 catheters. An analysis of the failure modes of this method indicated the need for stronger simulation models for capturing catheter deflections, the state of the art for which are described in the remainder of this section.

Mechanical Models for Needles: The field of virtual reality simulations of surgical procedures has a rich history of using mechanical modeling for needles (Fortmeier et al., 2015, 2016; DiMaio and Salcudean, 2005). Our method leverages results reported in two papers from 2006–2009 that compared different mechanical models for needles and determined the model that is most suited for brachytherapy needles (Goksel et al., 2009; Dehghan et al., 2006). In particular, these papers observe that brachytherapy needles are typically inserted through measured holes in a template (or base), bend due to numerous forces acting on them, including the interactions between the catheter and the tissue it passes through, movement of the template, and deformation of the tissue. They compared three mechanical models against a physical experiment (Fig. 4a), two classical FEM-based approaches and an angular spring model for deflection accuracy in a physical experiment. They then determined that an angular spring model (Goksel et al., 2009), which consists of a series of rigid bars connected by three angular springs with three corresponding degrees of freedom, i.e., angles α , β and γ , (see Fig. 4b), best models brachytherapy needles. In this model, equal length rod elements are connected by rotational springs for every deflection direction. The deflection of the catheter results from forces acting on the springs. A simpler model with only one deflection direction, α , is shown in Fig. 4c.

Physical experiments in these papers measured actual bending in brachytherapy needles by attaching different weights to the catheter tip while keeping the base fixed (Fig. 4a illustrates one such experiment) were set up in (Goksel et al., 2009; Dehghan et al., 2006). The actual deflection was compared to the prediction of the two FEM and the angular spring model, and the angular spring model was demonstrated to be the most efficient and accurate. We adapted this angular spring model with an one-dimensional approximation (see Fig 4c) that was initially presented in a workshop paper (Mastmeyer et al., 2015). Details of this model are presented in Sec. 3.1.1.

3. Materials and Methods

The method in a nutshell: We model a catheter as a series of short rods attached to one another using torsion springs that become more angulated from the tip of the catheter toward its base. Catheter segmentation in an MRI image is initiated by the user providing the location of a catheter tip followed by a constrained image-appearance based search for each of these short, thin, dark rods. A rod is labeled as part of the segmented catheter with the stipulation that increasing bending between adjacent rods is permitted from the tip toward the base, until the full length of the catheter is segmented (Fig. 4a). Following individual

segmentation of all the catheters, those intersecting one another are automatically identified and corrected in a post-processing refinement step.

Key notation used in the paper is summarized in the appendix: see page 37.

3.1. Angular Spring Model Calculus

Our model is a set of equations working in a sequence of 2D subspaces in 3D that allows the calculation of the geometry of each successive rod, given an initialization and a coordinate system for the catheter. In such a 2D subspace, let us for now assume a simple two-dimensional coordinate system with the catheter length extending in the x direction and deflection in the y direction. The insertion plane P is congruent to the y -axis at position 0 and the reference direction of an unbent catheter aligns with the zero x -axis.

We call it a *forward calculation* of the model when the fixed end of the catheter is used for initialization (Fig. 5), and a *backward calculation* when the free end or the catheter tip is used for initialization of the model calculations (Fig. 6).

3.1.1. Forward Calculation of Angular Spring Model—In the forward calculation, the start deflection angle α_0 is 0 and a given start force F_0 represents the rod-orthogonal component of the force, i.e. F_{tip} at that moment (Fig. 5). At that moment, F_0 equals F_{tip} . For the $i + 1^{st}$ rod, the following calculations are carried out: The deflection angle α_{i+1} is computed as:

$$\alpha_{i+1} = \frac{F_i}{k}, \quad (2)$$

the cumulative deflection α_{i+1}^{sum} is computed as:

$$\alpha_{i+1}^{sum} = \alpha_i^{sum} + \alpha_{i+1}, \quad (3)$$

and the orthogonal force component F_{i+1} as:

$$F_{i+1} = F_i \cdot \cos(\alpha_{i+1}^{sum}). \quad (4)$$

Based on the forward calculation, we define a continuous catheter model (Fig. 7) that maps a catheter tip location (characterized by a and d) into estimates of associated force at that tip location:

$$F_0^{mod}: \mathbb{R}^2 \rightarrow \mathbb{R}. \quad (5)$$

This allows estimation of catheter tip forces which are used in the next paragraphs as F_0 in Eq. (6).

3.1.2. Backward Calculation of Angular Spring Model—A backward calculation of the model has greater relevance to the problem at hand because we begin segmenting from the catheter tip. We need to estimate for the total deflection angle α_0^{sum} and the orthogonal final rod force F_0 derived from an estimate of the gravity direction force at the tip.

Using the terminology illustrated in Fig. 6, we perform the calculations as follows:

For the first rod ($i = 1$) we start with:

$$F_1 = \frac{F_0}{\cos(\alpha_0^{sum})}. \quad (6)$$

In subsequent rods, the steps are the reverse of the equations used in the forward calculation. The orthogonal force component is calculated as:

$$F_{i+1} = \frac{F_i}{\cos(\alpha_i^{sum})}, \quad (7)$$

The angle between adjacent rods is:

$$\alpha_{i+1} = \frac{F_{i+1}}{k} \quad (8)$$

The new cumulative angle between the reference axis and the $i + 1^{st}$ rod for re-iteration at Eq. (7) is calculated as:

$$\alpha_{i+1}^{sum} = \alpha_i^{sum} + \alpha_{i+1} \quad (9)$$

To compare our simulations to the findings of (Goksel et al., 2009; Dehghan et al., 2006) we simulated the results for eight catheters back and forth and found congruent deflections (using the same catheter stiffness). The results, shown in Fig. 7a, show this consistency, thereby confirming that the adapted and simplified bending model used here is valid for multiple catheters observed in physical experiments (Mastmeyer et al., 2015).

For the proposed model backwards iterations, we need to estimate the orthogonal final rod force F_0 and the total deflection angle α_0^{sum} at the catheter tip.

3.2. Model Estimation

First, we assume that the location of the base insertion plane P is known and a_{ref} is the declination angle vs. the scanner system axis (Figs. 2c, 6). Methods for identifying this plane are described in Sections 3.5.

Second, we assume the existence of a reference catheter $\vec{r} \perp P$ with zero forces acting on it.

Then we use the image data and start to walk backwards by a big step first to estimate the model for each catheter independently, as follows:

1. Specify t_0 , the tip, manually by clicking on it in the MRI, once per catheter. Methods for automating this step are discussed in the Future Works section.
2. Use an image-based 3D ray-casting algorithm as described in Sec. 3.3.2 to compute a long vector \vec{L}_{init} , an approximate estimate of the direction of the first small step rod of the catheter.
3. Use \vec{r} (with angle α_{ref} towards the scanner system-center-axis) and \vec{L}_{init} to estimate the rod deflection sum angle α_0^{sum}

$$\alpha_0^{sum} = \arccos \left(\|\vec{r}\| \cdot \|\vec{L}_{init}\| \right). \quad (10)$$

4. Compute the distance from the insertion plane a as the distance from the catheter grid base plane P .
5. Estimate the catheter deflection d from the tip to the reference catheter \vec{r} in normal direction as

$$d = \frac{a}{\cos(\alpha_{ref})} \cdot \sin(\alpha_0^{sum}). \quad (11)$$

The values for F_0 can be looked up using the computed values a and d in the model $F_0^{mod}(a, d)$ from Sec. 3.2 and the lower part of Fig. 7. Summing up, these steps initialize the model and mount the first 2D (a, d) -subspace with a aligned to the system axis \vec{r} and orthogonal to $(\vec{r}, \vec{L}_{init})$ (Fig. 6).

3.3. Combining Image-appearance of Catheters with Angular Spring Model Algorithm

We previously reported a cone search based method for catheter segmentation in which each catheter trajectory is represented as a Bezier curve, and the control points of each curve are automatically detected using an intensity-minimizing objective function that successfully captures the gray-level appearance of catheters in a small database with easy cases of 101 catheters (Pernelle et al., 2013). Here, we describe improvements in the intensity-based objective function and provide a strategy for how to combine it with the proposed angular spring model.

3.3.1. Enhanced Cone Search Using a Circular Laplacian Mask—Catheters are shaped like tubes in 3D which have circular cross-sections in 2D axial images. Their appearance is dark (signal voids) surrounded by brighter tissue in T2-weighted MRI images. In our image acquisitions, the highest spatial resolution is in the axial plane. Therefore, we developed a 3D filter walking along piecewise linear rays through the axial cross-sections. Within each axial image, this 2D filter uses a Laplacian-like mask with a strong response at the center of a dark circular disk surrounded by brighter intensities. Fig. 8 illustrates the catheter artifact, the circular mask, and its response in an example image.

$$G_{circ} = \begin{bmatrix} 1 & & 1 & & 1 \\ & \dots & \vdots & \dots & \\ 1 & \dots & -8 & \dots & 1 \\ & \dots & \vdots & \dots & \\ 1 & & 1 & & 1 \end{bmatrix} \quad (12)$$

The filter incorporates geometric information in 3D (being locally straight) and 2D (radius) about the used catheters. The three dots in the filter mask correspond to the radius of the catheters. This circular Laplacian mask has a peak response located with its center over an axial cross-section catheter artifact. Starting from a user click on the superior catheter tip, a ray search is performed for the best line candidate inside a small conic volume toward its base. The objective function integrates the results of convolving the axial 2D Laplacian-like filter G_{circ} of Eq. 12 with the image along the current ray. Mathematically, when searching in conic regions by ray casting, we look for superior to inferior line integrals minimizing the image intensity value $I(x)$ and taking the preferred gradient pattern into account. Once the best 3D line $\vec{l} = \overrightarrow{t_i c_{img}}$ with

$$c_{img} = \underset{c_{img}}{\operatorname{argmin}} \left(\int_{t_i}^{c_{img}} I(x) + G_{circ} * I(x) dx \right) \quad (13)$$

is found, the process is repeated using the accepted point c_{img} as new tip t_{i+1} for the next 3D cone search. Similar to our previous work, a Bezier curve with N control points can be already used at this juncture to combine the accepted points c_{img} into a trajectory for the catheter (Pernelle et al., 2013).

3.3.2. Using Cone Search to Initialize the Angular Spring Model and

Coordinate System—Both the analytical predictions of the angular spring model and an empirical analysis of the bending in manually segmented catheters show that most catheters are almost straight from the tip down to approximately halfway through their length (Fig. 4a). Based on this observation, we detect the top half of each catheter as \vec{L}_{init} (referred to as *superior half catheter*) by using the method described in Sec. 3.3.1. The direction of the *superior half* is used to initialize the angular spring model in Sec. 3.2 for one catheter.

Superior Half Catheter Search: We define the very first *large search cone* for model initialization only, with the user provided tip t_0 and height $\frac{a}{2}$, where a is the distance between t_0 and the base plane P that marks the inferior extent of the search space. Within this search cone with base point,

$$b_{init} = t_0 - \frac{a}{2} \cdot \|\vec{r}\| \quad (14)$$

and cone center axis vector $\vec{l}_1 = \overrightarrow{t_0 b_{init}}$ we compute the best long 3D line segment $\vec{L}_{init} = \overrightarrow{t_0 c_{img}} = \vec{l}_{img}$ that minimizes the 3D line integrals in Eq. (13). \vec{r} is the unbent catheter reference direction described earlier. The resultant line \vec{L}_{init} is then used in the model estimation in Eq. (10).

First Small Search Cone Catheter Search: Again, starting from the tip t_0 , the cone base center point b_0 of the first 3D *small search cone* is computed using the direction \vec{L}_{init} as

$$b_0 = t_0 + \frac{a}{N-1} \cdot \|\vec{L}_{init}\|, \quad (15)$$

where $\|\cdot\|$ denotes a normalized vector.

The point c_{img} found using the small cone with axis $\overrightarrow{t_0 b_0}$ is later used as t_1 , the tip of the rod of the second *small search cone*. This step also defines the first 3D small rod vector

$$\vec{l}_s = \overrightarrow{t_0 c_{img}} \quad (16)$$

and allows the initialization of a local rod coordinate system for the subsequent *small search cone* steps guided by the angular spring model.

Rod Coordinate Systems for the Angular Spring Model: As a replacement for 2 degrees of freedom (Goksel et al., 2009; Dehghan et al., 2006), we propose a zero-force rotational axial joint implicit in our local coordinate system definition. For efficiency reasons, we do not use more than one spring for the rod joints as proposed in (Goksel et al., 2009); however, our axial joint can rotate and provide the degrees of freedom needed to represent multiple bent catheters.

In the following iterations, using \vec{l}_s from Eq. 16, each rod line search step is accompanied by a local right-handed rod coordinate system (LRCS) $(\vec{n}_{loc}, \vec{d}_{loc}, \vec{a}_{loc})$ with

$$\vec{n}_{loc} = \|\vec{d}_{loc}\| \times \|\vec{a}_{loc}\|; \vec{d}_{loc} = \|\vec{n}_{loc}\| \times \|\vec{a}_{loc}\|; \vec{a}_{loc} = \|\vec{n}_{loc}\| \times \|\vec{d}_{loc}\| \quad (17)$$

in LPI (left to right, posterior to anterior, inferior to superior) directions. There is the catheter deflection plane normal \vec{n}_{loc} orthogonal to the 2D (a, d) -subspace (plane) for one step of the catheter bending simulation (Fig. 7). Then, a deflection direction \vec{d}_{loc} (d) and a reference direction \vec{a}_{loc} (cf. a , in Fig. 7) are defined. In each rod line search, they are defined anew. The adaptation of the LRCS and hence the $(\vec{a}_{loc}, \vec{d}_{loc})$ 2D subspace is triggered using the most recent rod vector $\vec{l}_s = t_j - t_{j-1}$ with t_j as the top of the current cone. It replaces \vec{a}_{loc} in Eq. 17, with the resulting coordinate system definition:

$$\vec{n}_{loc} = \|\vec{d}_{loc}\| \times \|\vec{l}_s\|; \dots \quad (18)$$

Therefore, the model catheter is able to simulate bending in more than one plane. This engineering approximation enables true 3D capability for the algorithm: stepwise, the LRCS and 2D subspace for the model iterations reorients slightly and allows the catheter to virtually bend in 3D.

3.3.3. Model-constraint-based Catheter Rod Search—With the top point of the cone t_i and the the base point as the center, the circular cone base (Fig. 9) can be reached using 3D catheter model backward calculations using a sequence of 2D subspaces. Deflection backward simulation steps take place for each search cone; the LRCS-2D-subspace is continuously adapted (see Sec. 3.3.2). In the rest of this paper, all points and vectors are 3D.

Model-based Rods and Search Cone Definition: With an initialized and running catheter deflection model in the subsequent cone searches, we use the model proposed cone base points b_{mod} (and rod proposals I_s) by adding a model-based step vector to the cone top t_i :

$$b_{mod} = t_i + d_{seg} \cdot \left(\|\vec{d}_{loc}\| \cdot \sin(\alpha_i^{sum}) + \|\vec{d}_{loc}\| \cdot \cos(\alpha_i^{sum}) \right). \quad (19)$$

The rod vector length $d_{seg} = a/(N-1)$ corresponds to the model-based cone center axis resp. rod defined by $\vec{l}_s = \overrightarrow{t_i b_{mod}}$. Now, we can begin the image-coupling based search for a rod proposal \vec{l}_{img} (see Fig. 9) and trade off against the model-based rod proposal \vec{l}_{mod} if so.

Constraint Fulfillment: In our current method, we use a distance constraint. Inside the model-proposed search cone, let the point c_{img} be found by the image-coupling described in Sec. 3.3.1. If the optimal point c_{img} is inside a pre-defined radial distance range d_{tol} from the model-proposed cone base point:

$$|c_{img} - b_{mod}| < d_{tol} \quad (20)$$

we accept it as the next cone top t_{i+1} and catheter defining point c_{acc} for the final catheter trajectory (see Fig. 9):

$$t_{i+1} = c_{acc} = c_{img} \quad (21)$$

and the catheter rod $\vec{l}_{acc} = \overrightarrow{t_i c_{acc}} = \overrightarrow{t_i c_{img}}$ is accepted (see Figs. 3 vs. 9).

Constraint Violation and Trade-off: However, with a point c_{img} deviating too far, an acceptable compromise point c_{acc} inside the constraint requirement is generated:

$$c_{acc} = b_{mod} + \|c_{img} - b_{mod}\| \cdot \min \left(d_{tol}, \frac{|c_{img} - b_{mod}|}{2} \right). \quad (22)$$

and the resulting catheter rod $\vec{l}_{acc} = \vec{t}_i c_{acc}$ is accepted (Fig. 9).

In this manner, a catheter path becomes a hybrid set of points between those proposed by the model and those proposed by the image features. All finally generated points are within the model constraints.

3.4. Identifying Erroneous Catheter Segmentations Based on Physically Improbable Pairwise Configurations

To complement the previous steps in which each catheter is segmented as an independent entity, in this step, the notion of physically feasible configurations of catheter-pairs is introduced into the method. This step can also be thought of as a quality-control measure for eliminating improbable trajectories that do not make sense in a collection of gynecologic brachytherapy catheters, even though they may as independent entities.

Analyzing segmentations obtained using the steps described thus far in the proposed method indicated three scenarios, illustrated in Fig. 10, where two catheters are close enough to one another that the trajectory for one catheter is derailed because of the artifact for the other catheter. Fig. 10 shows three scenarios of incorrect segmentations. The common reason for two catheter detections in the same place is that the distance between the trajectories of catheters is small and the artifact of one catheter is strong enough to affect the search of another catheter and mislead it. The scenarios shown correspond to three typical, error-prone catheter configurations, which can be detected and corrected later on.

The essence of the error correction step is to encode heuristics that govern the pairwise configurations of catheters. In particular, catheters that touch one another at some point and share volume are physically impossible. This typically happens when the artifact of one catheter is more salient than another and included in the same search cones space of the previous segmentation steps. We first identify the problematic pairs, then identify which catheter in each problem pair is causing the other catheter to be incorrectly segmented. In order to address the problem, we conceptually create a bright repulsion artifact (Fig. 11) in the underlying image that directs all others away from the problematic artifact, and finally re-segment the collection. This is implemented in the following four steps:

Step 1: Compute three morphologic metrics on catheters and catheter pairs to aid in understanding their relative geometry. The distance metric is used to detect conflicting catheters, while slope and curvature aim at finding the distracting catheter:

Distance metric ($D_a b$). Using the Euclidean distance $d(x, y) = |x - y|$ between two points x and y , the minimal pointwise symmetric distance between two dense point sets that comprise segmented catheters a and b is:

$$D_{ab} = d_{\min}(a, b) = \inf_{x \in a} \inf_{y \in b} d(x, y). \quad (23)$$

Values of distance metric less than the radius of a catheter, i.e. $D_{ab} < r_{cab}$ indicate potential interaction between the two catheters, and the likelihood that one catheter's search line is dragged into the artifact created by the other.

Slope metric (S_b). The difference between the direction measured by a vector \vec{b} of superior to inferior point $t_0 - t_{N-1}$ of a segmented catheter b and the average direction vector \vec{a} of the segmented catheter group from the previous step:

$$S_b = 1 - \frac{\vec{a} \cdot \vec{b}}{|\vec{a}| \cdot |\vec{b}|} \quad (24)$$

Catheters with higher S_b have higher probability of being incorrect.

Curvature metric (C_b). The curvature of an individual catheter b with N points and in between short line rod vectors \vec{l}_i is estimated by:

$$C_b = 1 - \frac{1}{N} \cdot \sum_{i=0}^{N-1} \frac{\vec{l}_i \cdot \vec{l}_{s,i+1}}{|\vec{l}_i| \cdot |\vec{l}_{s,i+1}|}. \quad (25)$$

Catheters with higher curvature have a higher probability of being incorrect.

Step 2. Investigate all catheter pairs where the distance D_{ab} between them is less than the radius of a catheter r_{cab} and classify them into scenarios 1, 2, or 3 from Fig. 10. The heuristics we use are shown below. Let a and b denote two conflicting catheters under consideration.

- Scenario 1. If $S_b \gg S_a$ or $C_b \gg C_a$, then the artifact from catheter a is causing the segmentation for b to be incorrect. This can be expressed as the following rule:

If $S_b - S_a > th_{s_1}$ or $C_b - C_a > th_{c_1}$, then b is incorrect.

Else If $S_b - S_a > th_{s_2}$ and $C_b - C_a > th_{c_2}$, then b is incorrect.

in which the four thresholds have been determined empirically and are provided later in the experiment setup section.

- Scenario 2. If the distance between the intersection point x and tip for a shorter catheter a is smaller than the radius of catheter r_{cab} catheter b is incorrect and the shaft of catheter a is causing the error. This scenario means the shorter catheter a is overlapping with a part of b 's wrongly detected

shaft (a is contained in b), and b is the incorrect one. This can be expressed as the following rule:

If $D_{tip_a x} < r_{cat}$ and tip_b is superior to tip_a , then b is incorrect.

- Scenario 3. Compute two line segments \vec{I}_a and \vec{I}_b between the intersection point x and tip of catheters a and b . The part of a catheter (yellow) that is more vertical corresponds to the incorrect one:

If $S_{\vec{I}_a} < S_{\vec{I}_b}$, then a is incorrect.

Step 3: De-emphasize the distracting catheter artifact from the underlying image by creating a repulsive artifact or constraint in the image as shown in Fig. 11.

Step 4: Repeat the segmentation of the erroneous catheter, detect errors, and iterate to convergence (no more changes).

In this way, the quality-control method described above iteratively resolves pair-wise conflicting catheter trajectories.

3.5. Study Parameters

In this section we describe the settings for parameters that have been mentioned in the algorithm described above.

The catheter model simulation and setup uses $N_{max} = 20$ rod segments for full length catheters (20 cm); lesser rod segments are automatically used for shorter catheters.

The catheter grid (Fig. 2a) that is used for insertion has holes with minimum spacing of 10 mm. Consistent with the definition of a critical maximum detection distance error below which a catheter can still be identified with the correct hole in the template base:

$$HD_{crit} = \frac{10 \text{ mm}}{2} - 1.6 \text{ mm} = 3.4 \text{ mm}. \quad (26)$$

Assuming a known location of the plane P , we can determine the declination angle α_{ref} (cf. Figs. 2c, 6) to encode the relative angle of the obturator inside the patient. The pre-processing method used to detect P is described below (Section 3.5) and from that AP declination for α_{ref} was calculated to be 22.5 degrees.

For the average insertion length of 74 mm, we used seven short rod search cones (one per cm) of equal height $d_{seg} = a/(N-1)$ to allow for 3D bending and a number of $N = 8$ path points for Bezier approximation.

We choose $k = 2050 \mu N/m$ as we used stiffer 16 Gauge catheters than described in (Goksel et al., 2009). The radius of the circular cone base r_{cone} was set to 20 mm to account for significant bending and to evaluate the image coupling influence against the model. The tolerated deviation from the model d_{tol} was chosen 1 mm.

For the identification of erroneous catheter (Sec. 3.4) we use $th_{S1} = 0.02$, $th_{S2} = 0.01$, $th_{C1} = 0.015$ and $th_{C2} = 0.005$ that have been determined empirically.

3.5.1. Identification of P in this Experiment—The field of view of the acquired MRI volumes was standardized such that (1) the center of the obturator was in line with the scanner system axis (template in the middle of the axial cross-sections), and (2) the template was included in the volume. In a pre-processing step, P was interactively identified in all MRI volumes, and an average location (center of the template) and orientation for P were derived relative to the inferior-most axial slice of the volume.

There are additional options for the detection of P that we considering concurrently and these are discussed in (Section 6.1).

3.6. MRI Data and Brachytherapy Hardware

Images: This segmentation method was evaluated on MRI scans of 54 gynecologic cancer patients who were treated using 760 HDR brachytherapy catheters. All catheter insertions and scans were performed in the AMIGO suite at Brigham and Women’s Hospital, Boston, USA, between 2011 and 2016. The MRI scans were acquired on a 3 Tesla “Magnetom Verio” scanner (Siemens Healthcare, Erlangen, Germany) using the three-dimensional T2/FSE protocol (Siemens SPACE, TR/TE=3000/160 ms, $0.4 \times 0.4 \times 1.0 \text{ mm}^3$). The field of view of the volumes was standardized by guidelines with the center of the obturator in line with the scanner system axis and the template base included in the MRI images. Reference segmentations for all 760 catheters from 54 patients were manually performed by a physician using the 3D Slicer open source software.

Insertion Hardware: The Syed-Neblett template (shown in Fig. 2a) with 56 holes arranged in concentric circles, with 10 mm spacing between them, is used at our institution for this procedure and in this study (Viswanathan et al., 2011; Kapur et al., 2012). An obturator is firmly attached to the template base and sutured to the perineum of the patient. What is referred to as a “catheter” in this paper consists of a 1.6 mm (16G) diameter, radius $r_{cat} = 0.8$ mm, hollow plastic sheath with a tungsten-alloy stylet inside. The combination appears dark (signal void) on the MRI images. We measured a mean catheter insertion depth of 74 mm and an average number of catheters per patient of 14 ± 7 .

4. Accuracy and Precision Experiments

To quantify the performance of our segmentation method, we designed an *in-silico* experiment to measure its accuracy against a reference standard. This experiment consists of a simulated user interactively identifying the tips of all catheters in an MRI scan, the proposed method automatically segmenting the entire catheter trajectories, and a Hausdorff Distance based calculation of the accuracy of the automatic segmentation against the reference standard.

Since our segmentation method depends on user-interaction to obtain the tip, we designed a second *in-silico* experiment to measure the precision of the method. This experiment consists of a simulation of four users by randomly displacing the tip initialization by 0.8 mm

(radius of the catheter) from the optimally centered tip position used in the accuracy experiments. We then measure the percent coefficient of variation (%CV) per patient.

The concepts of accuracy and precision used in the context of this paper are an international ISO standard (ISO, International Organization for Standardization), and statistical analysis was carried out using the software package SPSS 23 (IBM, Armonk, NY, USA).

The aim of our segmentation method are outcomes with high user precision (small variation) and high accuracy (trueness). In the future, when we are able to eliminate the need for an interactive tip initialization, the need for high user precision will be less important.

4.1. Accuracy calculation using Hausdorff Distance

After manual initialization of each catheter tip, an automatic segmentation is performed, and the Hausdorff Distance (HD) is used as the metric for evaluating the accuracy of a catheter against its reference segmentation (Huttenlocher et al., 1993). Computed as shown below, it quantifies the two-sided maximal Euclidean distance between two catheter segmentations and, therefore, captures the maximum disagreement between them:

$$HD_{a,b} = d_{HD}(a,b) = \max\{\sup_{x \in a} \inf_{y \in b} d(x,y), \sup_{y \in b} \inf_{x \in a} d(x,y)\}. \quad (27)$$

4.2. Precision calculation on Simulated Tip Clicks

We simulate four users by randomly displacing the tip initialization by 0.8 mm (radius of the catheter) from the optimal tip position used in the accuracy experiments. We then measure the percent coefficient of variation (%CV) for a patient p of N_P patients comparing the users u results from the Hausdorff Distances for a catheter n $HD_{p,u,n}$. The %CV concept describes standard deviations unrelated to their means, renders them comparable and is an accepted standard in precision studies (Gluer et al., 1995).

First, we calculate the mean Hausdorff error $\overline{HD}_{p,u}$ summing up all catheter results. Next, integrating the user dimension, the dimensionless %CV $_p$ per patient with sample standard deviation indicated by \widetilde{HD}_p :

$$\%CV_p = \frac{\widetilde{HD}_p}{\overline{HD}_p} \cdot 100 \quad (28)$$

Then, we estimate the average deviation in mm as:

$$\widetilde{D}_{\%CV} = \frac{\overline{HD} \cdot \overline{\%CV}}{100} \quad (29)$$

with $\bar{X} = \frac{1}{N_P} \sum_{p=1}^{N_P} X_p$ as the sample mean and \tilde{X} as the sample standard deviation, eliminating the final patient dimension.

The results are expressed again using the more conservative root mean square (RMS) percent average coefficient of variation (Gluer et al., 1995):

$$\%CV_{RMS} = \sqrt{\frac{1}{N_P} \cdot \sum_{p=1}^{N_P} (\%CV_p)^2} \quad (30)$$

These are restated as RMS mean deviation [mm] (precision error) in our four simulated user tries:

$$\tilde{D}_{CV_{RMS}} = \frac{\overline{HD} \cdot \%CV_{RMS}}{100} \quad (31)$$

5. Results

In this section we present the accuracy and precision of our method, compare these results to previous work, and discuss limitations of the method as well as directions for future work.

5.1. Accuracy

Qualitative accuracy results of the proposed method are presented in Fig. 12 for visual inspection. The top two rows show excellent agreement between segmentation (green) and reference segmentations (cyan) of a catheter group in a representative patient. The bottom row in the same figure illustrates the value of combining both image and model information in the segmentation process; a particular catheter that showed poor agreement with the reference segmentation when only image or only model constraints are used, is segmented accurately when both model and image information are combined.

Quantitative accuracy results for 760 catheters are shown in Table 1. Accuracy is measured as the Hausdorff Distance (HD) between the output of the proposed segmentation method and the expert-provided reference segmentations of the catheters. 709 out of 760 (or 93%) catheters are segmented with a clinically acceptable accuracy of $HD \leq 3.4$ mm (Eq. 26), and the overall mean HD is 1.49 mm with a standard deviation of 2.04 mm.

5.2. Precision

Precision measurements are shown in Table 2. The mean HD errors of the experiments and user tries are shown in the left most column, \overline{HD} . The RMS-%CV (18.66%) projects to a RMS deviation, i.e. "precision error", of ± 0.29 mm, and a majority of segmentation errors are below $HD_{crit} = 3.4$ mm, i.e., $1.57 + 3 \cdot 0.29 = 2.44$.

5.3. Speed

The average segmentation time for a single catheter was 3 seconds⁴ on a standard personal computer with a single i7 3 Ghz processor and 4 GB RAM.

5.4. Comparison

As noted in Section 2, to the best of our knowledge, the state of the art for catheter segmentation from MRI is our previous work, which was performed on a much smaller set of images and does not contain an angular spring model for catheters (Pernelle et al., 2013). Below, we present a quantitative comparison of the accuracy and precision of the proposed method to the previous work.

Accuracy Comparison with (Pernelle et al., 2013) is shown in Table 3 and Fig. 13. In Table 3, the proposed method shows a consistent improvement in accuracy mean and standard deviation over the comparison method. It shows an improvement in identification of catheters within the critical distance of 3.4 mm (Eq. 26) from 88% to 93% which corresponds to a reduction in outliers (HD > 4 mm) from 95 to 51. The differences are convincing as shown by a Wilcoxon Signed Rank Test ($p < 0.062$).

Precision comparison demonstrates consistently more precise results than the comparison method, as shown in Table 4 and Fig. 14. The %CV differences are statistically significant as shown by a paired t-test ($p < 0.006$). Fig. 14 shows HD darts charts for 760 catheters on radial lines displaying the errors on a logarithmic scale where the outer ring corresponds to 100 mm and the middle ring to 10 mm, from four simulated user tries. Visual inspection of this figure indicates that the proposed method has a "tighter" spread of accuracy around the mean than the comparison method, and hence a higher precision.

6. Discussion

In this work, we used unique data, a new methodology, and evaluation to address the increasingly important problem of needle localization or catheter segmentation in MRI images. This work is timely because the use of MRI for placement of therapy delivery catheters is leading to improved outcomes for patients, especially in gynecologic cancer (Damato and Viswanathan, 2015). To the best of our knowledge, this is the first comprehensive accuracy and precision study on catheter detection on patient MRI images. The results are promising and facilitate intraoperative or postoperative identification.

6.1. Identification of P

The identification of the plane P is currently a research project using the embedding of special material markers inside the template hardware that are highlighted in MRI and can be segmented by simple thresholding followed by a plane regression. These markers were not consistently available for this work, and a standard average plane P based on our patient population was used.

⁴Python implementation

Thus, the experiments are independent from an optimized identification of P . We plan to complete the work on this topic and use the advanced identification method together with the method shown here.

6.2. Robustness

In Section 3.5, we have listed the key parameters of the proposed method, provided an intuition for their usage, and their default values. The default values serve well the encountered situation of a mean 7.4 cm catheter insertion length in this application. These parameters have shown robustness for three different imaging protocols in a previous publication (Mastmeyer et al., 2015).

While attention was paid to not overfit the data while selecting individual parameter settings, a formal study of the robustness of the system to different MRI sequences and insertion hardware (catheters, templates) has not been performed yet. In the future, as MR-guided HDR brachytherapy of gynecologic cancer gains wider clinical acceptance, we hope to test our algorithm on data from additional sites to demonstrate robustness.

6.3. Clinical Performance Requirements

Our long-term goal for this research project is for the resultant method to be as easy to use, robust, and accurate as what is available commercially for use with CT images. In the presented study, we have demonstrated the feasibility of performing this task based on criteria that were developed in discussions with clinical partners:

- **fast and easy:** The method should take up to 2–3 seconds per catheter, and up to 1–2 "easy" mouse clicks from the user.
- **manual override:** An easy to use interactive option should exist to override incorrect automatic segmentations.
- **90%:** The automated method should result in segmentations comparable to human segmentation over 90% of the time.

In the future, as we move this work closer to prospective clinical deployment, the segmentation accuracy requirements will be refined and stated in terms of the impact on radiation dose to the tumor and adjacent normal tissue. In order to do this, dose-calculation studies will be performed, in partnership with radiation physicists, to relate deviations in segmentation of the catheter to the resultant uncertainties in dose calculation. That will allow us to determine realistic clinical performance requirements.

6.4. Alternative Technologies

As of today, clinical research that leverages MRI for brachytherapy catheter insertion or treatment planning, does not rely on MRI for catheter segmentation (Kamran et al., 2017). It acquires a CT scan which is then registered to the MRI, but segmentation of the catheters is performed in the CT. Completely different technology has also been explored to circumvent the need for image-based segmentation of catheters by using custom tracking hardware embedded in each catheter to enhance its signal in the MRI image (Wang et al., 2015a,b). The goal of this work is provide a robust catheter segmenter from MRI images to the HDR

brachytherapy community so that it can make their workflow more effective and efficient, and in the long term ultimately eliminate the need for a CT scan or tracking hardware simply for the purpose of segmenting catheters.

6.5. Generalizability

The proposed catheter model is readily generalizable to include different types of locally straight catheters or needles that are introduced percutaneously into the body through a rigid base or template, and may bend and cross each other deeper into the body. It is straightforward to generalize the image-coupling component of the method to other volumetric (MR and CT) images. Preliminary results indicate promise in applying it to MR-guided prostate biopsy needle segmentation, a procedure which uses different imaging protocols and insertion hardware (Ziaei et al., 2017).

However, generalizing the method for use with ultrasound and fluoroscopic images, extremely important clinical workhorse modalities for percutaneous needle-based interventions, will involve incorporation of modality-specific image-coupling objective functions to capture the grayscale appearance of needles in each case (Hrinivich et al., 2017; Wang et al., 2010).

Within the gynecologic HDR brachytherapy application, the quantitative results of this study are applicable to the Syed-Neblett template which has a minimum 10 mm spacing between holes, and generalization for different templates with more closely spaced holes (such as the MUPIT template (Bansal et al., 2016)) will need dedicated experiments.

6.6. Future Work

Our near-term plans include a multi-user study with four physicians providing tip initialization rather than a simulation. The true user clicks then can be used to determine realistic tip click displacements distributions - which then could be used for exhaustive Monte-Carlo-Simulations. Right now, two simulated clicks can be separated at most by 1.6 mm, i.e. 4 voxels in the axial plane, and are placed on the border of the catheter artifacts, which is a variation borderline to clearly wrong clicks and quite challenges our method in the evaluation. A knowledgeable user would click more in the middle of the artifact, not on the border.

Since completing the work reported in this paper where features to encode catheter artifacts were "hand crafted" based on the authors' observations of several examples, we have begun investigating the training of deep convolutional neural networks (CNN) to the task by leveraging insights from (Ghafoorian et al., 2017; Mehrtash et al., 2017). This initiative covers tip detection which could be used to seed the presented method, as well as an alternative catheter detection method.

6.7. Conclusion

We have proposed a novel method that applies a mechanically augmented, image-based, catheter model to deliver efficient, accurate, and precise catheter segmentation in a feasibility study for MRI-guided, high dose rate brachytherapy treatments for gynecologic

cancer. This method is the first to be evaluated on a large database of clinical MRI scans containing 760 catheters and demonstrates favorable 93% accuracy and statistically highly significant improvement in precision over previous work.

References

- Aboofazeli, M., Abolmaesumi, P., Mousavi, P., Fichtinger, G. A new scheme for curved needle segmentation in three-dimensional ultrasound images, in: *Biomedical Imaging: From Nano to Macro*, 2009. ISBI'09. IEEE International Symposium on; IEEE; 2009. p. 1067-1070.
- American Cancer Society. [Accessed on 05/08/2016] Cancer facts and figures. 2015. URL: <http://www.cancer.org/research/cancerfactsstatistics/cancerfactsfigures2015/index>
- Aylward SR, Bullitt E. Initialization, noise, singularities, and scale in height ridge traversal for tubular object centerline extraction. *IEEE transactions on medical imaging*. 2002; 21:61–75. [PubMed: 11929106]
- Bansal I, Panda D, Rathi A, Anand A, Bansal A. Rationale, indications, techniques and applications of interstitial brachytherapy for carcinoma cervix. *Asian Journal of Oncology*. 2016; 2:69–78. DOI: 10.4103/2454-6798.197374
- Czerwinski RN, Jones DL, O'Brien WD. Detection of lines and boundaries in speckle images-application to medical ultrasound. *IEEE transactions on medical imaging*. 1999; 18:126–136. [PubMed: 10232669]
- Damato AL, Viswanathan AN. Magnetic resonance-guided gynecologic brachytherapy. *Magnetic resonance imaging clinics of North America*. 2015; 23:633–642. [PubMed: 26499280]
- Daoud MI, Rohling RN, Salcudean SE, Abolmaesumi P. Needle detection in curvilinear ultrasound images based on the reflection pattern of circular ultrasound waves. *Medical physics*. 2015; 42:6221–6233. [PubMed: 26520715]
- Dehghan, E., Goksel, O., Salcudean, S. A comparison of needle bending models. In: Larsen, R.Nielsen, M., Sporning, J., editors. *Medical Image Computing and Computer-Assisted Intervention - MIC-CAI 2006*. Springer Berlin Heidelberg; 2006. p. 305-312. volume 4190 of *Lecture Notes in Computer Science*
- DiMaio S, Kacher D, Ellis R, Fichtinger G, Hata N, Zientara G, Panych L, Kikinis R, Jolesz F. Needle artifact localization in 3t mr images. *Studies in Health Technology and Informatics*. 2005; 119:120.
- DiMaio SP, Salcudean SE. Interactive simulation of needle insertion models. *IEEE transactions on biomedical engineering*. 2005; 52:1167–1179. [PubMed: 16041980]
- Duda RO, Hart PE. Use of the hough transformation to detect lines and curves in pictures. *Communications of the ACM*. 1972; 15:11–15.
- Fortmeier D, Mastmeyer A, Schröder J, Handels H. A virtual reality system for ptd simulation using direct visuo-haptic rendering of partially segmented image data. *IEEE journal of biomedical and health informatics*. 2016; 20:355–366. [PubMed: 25532197]
- Fortmeier D, Wilms M, Mastmeyer A, Handels H. Direct visuo-haptic 4d volume rendering using respiratory motion models. *IEEE transactions on haptics*. 2015; 8:371–383. [PubMed: 26087498]
- Frangi, AF., Niessen, WJ., Vincken, KL., Viergever, MA. *International Conference on Medical Image Computing and Computer-Assisted Intervention*. Springer; 1998. Multiscale vessel enhancement filtering; p. 130-137.
- Fu, H., Xu, Y., Lin, S., Wong, DWK., Liu, J. *International Conference on Medical Image Computing and Computer-Assisted Intervention*. Springer; 2016. Deepvessel: Retinal vessel segmentation via deep learning and conditional random field; p. 132-139.
- Ghafoorian M, Mehrtash A, Kapur T, Karssemeijer N, Marchiori E, Pesteie M, Guttman CR, de Leeuw FE, Tempany CM, van Ginneken B, et al. Transfer learning for domain adaptation in mri: Application in brain lesion segmentation. 2017 arXiv preprint arXiv:1702.07841.
- Gluer CC, Blake G, Lu Y, Blunt B, Jergas M, Genant H. Accurate assessment of precision errors: How to measure the reproducibility of bone densitometry techniques. *Osteoporosis International*. 1995; 5:262–270. [PubMed: 7492865]

- Goksel O, Dehghan E, Salcudean S. Modeling and simulation of flexible needles. *Medical Engineering & Physics*. 2009; 31:1069–1078. [PubMed: 19674926]
- Grover S, Harkenrider MM, Cho LP, Erickson B, Small C, Small W, Viswanathan AN. Image guided cervical brachytherapy: 2014 survey of the american brachytherapy society. *International Journal of Radiation Oncology* Biology* Physics*. 2016; 94:598–604.
- Han K, Viswanathan AN. Brachytherapy in gynecologic cancers: Why is it underused? *Current oncology reports*. 2016; 18:1–5. [PubMed: 26694922]
- Hao X, Zygmunt K, Whitaker RT, Fletcher PT. Improved segmentation of white matter tracts with adaptive riemannian metrics. *Medical image analysis*. 2014; 18:161–175. [PubMed: 24211814]
- Honnorat, N. PhD thesis. Ecole Centrale de Paris, CVC laboratory; 2013. Curvilinear Structures Segmentation and Tracking in Interventional Imaging.
- Honnorat N, Vaillant R, Paragios N. Guide-wire extraction through perceptual organization of local segments in fluoroscopic images. *Medical Image Computing and Computer-Assisted Intervention–MICCAI*. 2010; 2010:440–448.
- Hrinivich WT, Hoover DA, Surry K, Edirisinghe C, Montreuil J, D’Souza D, Fenster A, Wong E. Simultaneous automatic segmentation of multiple needles using 3d ultrasound for high-dose-rate prostate brachytherapy. *Medical Physics*. 2017; 44:1234–1245. [PubMed: 28160517]
- Huttenlocher D, Klanderman G, Rucklidge W. Comparing images using the hausdorff distance. *Pattern Analysis and Machine Intelligence, IEEE Transactions on*. 1993; 15:850–863.
- ISO, International Organization for Standardization,. Iso-norm 5725-1:1994: Accuracy (trueness and precision) of measurement methods and results - part 1: General principles and definitions.
- Jolesz, F. *Intraoperative Imaging and Image-Guided Therapy*. Springer Science & Business Media; 2014.
- Kamran SC, Manuel MM, Cho LP, Damato AL, Schmidt EJ, Tempany C, Cormack RA, Viswanathan AN. Comparison of outcomes for mr-guided versus ct-guided high-dose-rate interstitial brachytherapy in women with locally advanced carcinoma of the cervix. *Gynecologic Oncology*. 2017; 145:284–290. [PubMed: 28318644]
- Kapur T, Egger J, Damato A, Schmidt EJ, Viswanathan AN. 3-t mr-guided brachytherapy for gynecologic malignancies. *Magnetic resonance imaging*. 2012; 30:1279–1290. [PubMed: 22898699]
- Kerrien E, Yureidini A, Dequid J, Duriez C, Anxionnat R, Cotin S. Blood vessel modeling for interactive simulation of interventional neuroradiology procedures. *Medical image analysis*. 2017; 35:685–698. [PubMed: 27788384]
- Lesage D, Angelini ED, Funka-Lea G, Bloch I. Adaptive particle filtering for coronary artery segmentation from 3d ct angiograms. *Computer Vision and Image Understanding*. 2016; 151:29–46.
- Litjens G, Kooi T, Bejnordi BE, Setio AAA, Ciompi F, Ghafoorian M, van der Laak JA, van Ginneken B, Sánchez CI. A survey on deep learning in medical image analysis. 2017 arXiv preprint arXiv: 1702.05747.
- Manniesing R, Schaap M, Rozie S, Hameeteman R, Vukadinovic D, van der Lugt A, Niessen W. Robust cta lumen segmentation of the atherosclerotic carotid artery bifurcation in a large patient population. *Medical image analysis*. 2010; 14:759–769. [PubMed: 20605737]
- Mastmeyer, A., Pernelle, G., Barber, L., Pieper, S., Fortmeier, D., Wells, S., Handels, H., Kapur, T. Model-based catheter segmentation in MRI-images. *MICCAI Workshop on Interactive Medical Image Computing, IMIC 2015, 18th International Conference on Medical Image Computing and Computer-Assisted Intervention - MICCAI; 2015; München*. 2015. p. 110-118.
- Mehrtash A, Pesteie M, Hetherington J, Behringer PA, Kapur T, Wells WM, Rohling R, Fedorov A, Abolmaesumi P. Deepinfer: open-source deep learning deployment toolkit for image-guided therapy. *SPIE Medical Imaging, International Society for Optics and Photonics*. 2017:101351K–101351K.
- O’Donnell LJ, Westin CF. Automatic tractography segmentation using a high-dimensional white matter atlas. *IEEE transactions on medical imaging*. 2007; 26:1562–1575. [PubMed: 18041271]
- Okazawa S, Ebrahimi R, Chuang J, Rohling R, Salcudean S. Methods for segmenting curved needles in ultrasound images. *Medical Image Analysis*. 2006; 10:330–342. URL: <http://>

- www.sciencedirect.com/science/article/pii/S136184150600003X. special Issue on The Second International Workshop on Biomedical Image Registration (WBIR'03). [PubMed: 16520082]
- Pakhomov D, Premachandran V, Allan M, Azizian M, Navab N. Deep residual learning for instrument segmentation in robotic surgery. 2017 arXiv preprint arXiv:1703.08580.
- Pernelle, G., Mehrtash, A., Barber, L., Damato, A., Wang, W., Seethamraju, R., Schmidt, E., Cormack, RA., Wells, W., Viswanathan, A., Kapur, T. Validation of catheter segmentation for mr-guided gynecologic cancer brachytherapy. In: Mori, K.Sakuma, I.Sato, Y.Barillot, C., Navab, N., editors. Medical Image Computing and Computer-Assisted Intervention - MICCAI 2013. Springer Berlin Heidelberg; 2013. p. 380-387. volume 8151 of *Lecture Notes in Computer Science*
- Pourtaherian, A., Mihajlovic, N., Zinger, S., Korsten, HH., de With, PH., Huang, J., Ng, GC. Automated in-plane visualization of steep needles from 3d ultrasound data volumes. Ultrasonics Symposium (IUS), 2016 IEEE International; IEEE; 2016. p. 1-4.
- Qiu W, Yuchi M, Ding M, Tessier D, Fenster A. Needle segmentation using 3d hough transform in 3d trus guided prostate transperineal therapy. Medical physics. 2013; 40:042902. [PubMed: 23556924]
- Rafat Zand K, Reinhold C, Haider MA, Nakai A, Rohoman L, Maheshwari S. Artifacts and pitfalls in mr imaging of the pelvis. Journal of Magnetic Resonance Imaging. 2007; 26:480-497. [PubMed: 17623875]
- Schaap, M., Smal, I., Metz, C., van Walsum, T., Niessen, W. Bayesian tracking of elongated structures in 3d images. Biennial International Conference on Information Processing in Medical Imaging; Springer; 2007. p. 74-85.
- Schneider M, Hirsch S, Weber B, Székely G, Menze BH. Joint 3-d vessel segmentation and centerline extraction using oblique hough forests with steerable filters. Medical image analysis. 2015; 19:220-249. [PubMed: 25461339]
- Song S, Cho N, Iordachita I, Guion P, GF, Kaushal A, Camphausen K, Whitcomb L. Biopsy catheter artifact localization in mri-guided robotic transrectal prostate intervention. IEEE Trans Biomed Eng. 2012; 59:1902-11. [PubMed: 22481805]
- Sultana S, Blatt J, Gilles B, Rashid T, Audette M. Mri-based medial axis extraction and boundary segmentation of cranial nerves through discrete deformable 3d contour and surface models. IEEE Transactions on Medical Imaging. 2017
- Tempany C, Jayender J, Kapur T, Bueno R, Golby A, Agar N, Jolesz FA. Multimodal imaging for improved diagnosis and treatment of cancers. Cancer. 2015; 121:817-827. [PubMed: 25204551]
- Vandini A, Glocker B, Hamady M, Yang GZ. Robust guidewire tracking under large deformations combining segment-like features (seglets). Medical image analysis. 2017; 38:150-164. [PubMed: 28391062]
- Viswanathan, AN., Kirisits, C., Erickson, B., Pötter, R. Gynecologic radiation therapy. Springer; 2011.
- Viswanathan, Akila N. [Accessed on 05/10/2017] Clinical trial nct02993900: Image-guided gynecologic brachytherapy. 2016. URL: <https://clinicaltrials.gov/ct2/show/NCT02993900>
- Wang, P., Marcus, P., Chen, T., Comaniciu, D. Using needle detection and tracking for motion compensation in abdominal interventions. 2010 IEEE International Symposium on Biomedical Imaging: From Nano to Macro; 2010. p. 612-615.
- Wang W, Dumoulin CL, Viswanathan AN, Tse ZT, Mehrtash A, Loew W, Norton I, Tokuda J, Seethamraju RT, Kapur T, et al. Real-time active mr-tracking of metallic stylets in mr-guided radiation therapy. Magnetic resonance in medicine. 2015a; 73:1803-1811. [PubMed: 24903165]
- Wang W, Viswanathan AN, Damato AL, Chen Y, Tse Z, Pan L, Tokuda J, Seethamraju RT, Dumoulin CL, Schmidt EJ, et al. Evaluation of an active magnetic resonance tracking system for interstitial brachytherapy. Medical physics. 2015b; 42:7114-7121. [PubMed: 26632065]
- Wink O, Niessen WJ, Viergever MA. Multiscale vessel tracking. IEEE Transactions on Medical Imaging. 2004; 23:130-133. [PubMed: 14719694]
- Ziaei A, Mehrtash A, Pernelle G, Mastmeyer A, Fedorov A, Tuncali K, Tempany C, Kapur T. Needle trajectory segmentation for mri-guided prostate biopsy. 2017 submitted to RSNA conference 2017.

Appendix

Notation Used in the Paper

\overline{HD}	A mean value from multiple HD measurements.
$\widetilde{HD}, \tilde{D}$	A deviation joined to a HD mean value: standard deviation or precision error.
★	Image template mask folding operator.
$ \cdot $	Length of a vector.
$\ \cdot\ $	A normalized vector.
α_{ref}	The assumed angle between the reference catheter \vec{r} and the scanner system z-axis.
α_i	The deflection angle between the i^{th} rod and the previous one.
G_{circ}	Circular Laplacian-based mask for catheter artifacts.
α_i^{sum}	Total deflection angle of the i^{th} rod from a reference direction of a non-bent catheter with zero force at the tip.
a	Orthogonal distance from clicked tip to base plane P .
\vec{a}	Average vector of a segmented catheter group.
\vec{a}_{loc}	Insertion oriented base vector of the LRCS.
\vec{b}	Vector of superior to inferior point $t_0 - t_{N-1}$ of a segmented catheter b .
b_{init}	Base point of a large search cone for half catheter search (model initialization).
b_i	i^{th} rod base point of the sequence of small search cones.
b_{mod}	Catheter model proposed base point of a small search cone.
C_a	Curvature metric of a catheter.
c_{img}	Next search cone top found by image-coupling.
c_{acc}	Accepted (trade-off) rod end point (next search cone top).
CV	Coefficient of variation.
$\%CV$	Coefficient of variation, i.e. precision error in %.
d	Deflection of the catheter.
$d...(a, b)$	A distance metric (min or HD) between two catheters a, b .

\vec{d}_{loc}	Deflection oriented base vector of the LRCS.
d_{seg}	Height of a small search cone.
d_{tol}	Tolerance for an image-based rod end point to deviate from the model-proposed end point.
\tilde{D}_{CVRMS}	RMS precision error in <i>mm</i> .
$D_{a b}$	Minimal distance between two point sets, e.g. catheters.
F_i	Orthogonal end point forces on the i^{th} rod.
F_0^{mod}	Model based orthogonal force on the most superior rod.
F_{tip}	Gravity end point forces on the superior rod.
HD	Hausdorff distance.
$HD_{a b}$	Bidirectional Hausdorff distance between two point sets, e.g. catheters.
i	Current rod index ($i=0$: rod at tip).
$I(x)$	The image under work.
k	The physical angular spring stiffness coefficient of a single joint in the catheter.
\vec{L}_{init}	First large medial axis of search cone.
$\vec{l}_{...}$	Calculated line segment.
\vec{l}_l	First large medial axis of search cone (model initialization).
\vec{l}_{acc}	Accepted (trade-off) rod vector.
\vec{l}_{img}	Image-coupling proposed rod vector.
\vec{l}_{mod}	Model-bases proposed rod vector, cf. \vec{l}_s .
\vec{l}_s	Small rod vector (medial axis of search cone).
\vec{l}_i	The i^{th} small rod vector (medial axis of search cone).
LRCS	Local rod coordinate system (right-handed).
\vec{n}_{loc}	Base vector of the LRCS normal to the others.
N	The number of small search cones or rods.
N_{max}	The number of rods or search cones for a maximum length catheter.
N_p	The number of patients used in the study.

P	The plane of the fixture through which the catheters are inserted into the body.
\vec{r}	The reference direction of an unbent catheter $\vec{r} \perp P$.
r_{cat}	Radius of a catheter.
r_{cone}	Radius of a search cone.
RMS	Root mean squared.
S_a	Slope metric of a catheter.
t_i	i th rod tip point of the sequence of small search cones.
tip_a	The tip of a catheter a , i.e. t_0 of it.
th_{S1}	Threshold for the slope metric S .
th_{S2}	Threshold for the slope metric.
th_{C1}	Threshold for the curvature metric C .
th_{C2}	Threshold for the curvature metric.
x	The most superior interaction point of a catheter pair.

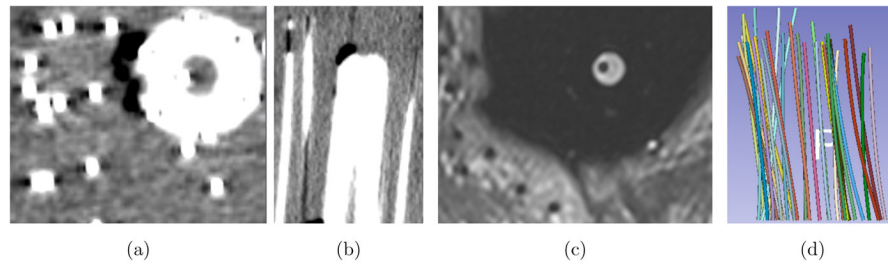


Figure 1.

Typical image examples with catheters and obturator: (a, b) Examples of an axial (a) and sagittal (b) CT images with distinct bright obturator area and bright catheter artifacts caused by the metallic catheter inlay. Some catheters in (a) touch each other. In (b) the leftmost catheter also shows its easily identifiable tip artifact as a bright spot. (c) Example of an axial MRI image with dark obturator area and eight dark catheter artifacts [R1.3]. They are hard to spot and are our target in a stack of axial slices. (d) A 3D display (anterior) of a patient with many (up to 40) colored catheters inserted.

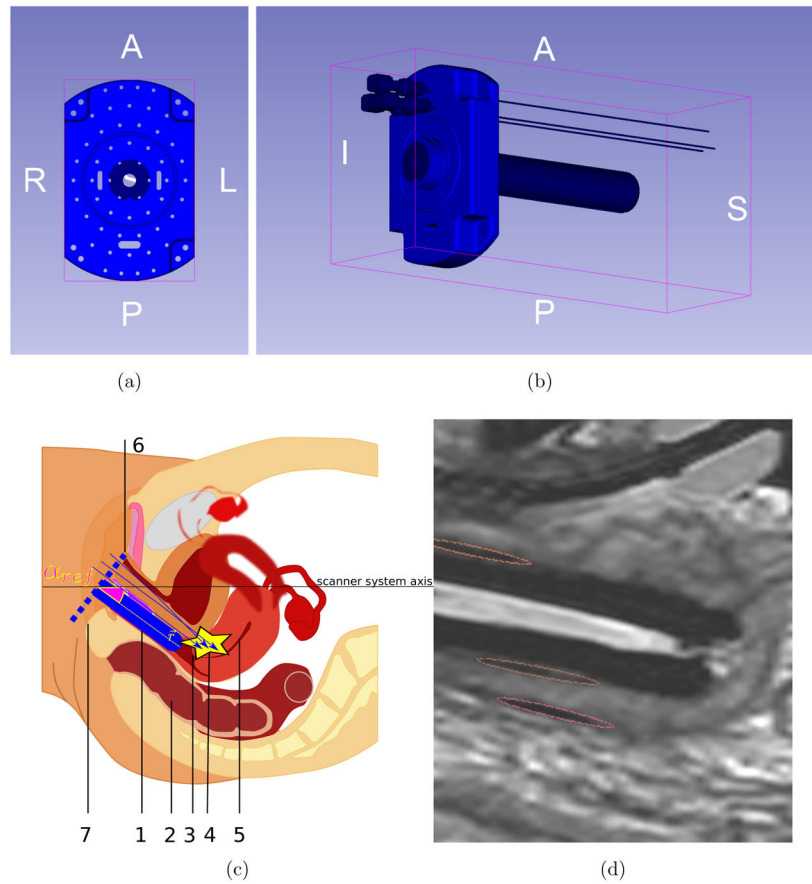


Figure 2.

[R1.3,R2.1,R3.5] This figure illustrates HDR brachytherapy insertion hardware, gynecologic anatomy, and MRI images. The template grid is shown in (a). The thick cylindrical obturator and three catheters inserted through the template are shown in (b). Patient anatomy with inserted hardware is shown in (c) – perineum where the template is attached (7), cervix (3), target lesion (4), uterus (5), anus (2), and insertion hardware (6 and 1 – in blue). A sagittal MRI image with dark obturator in the middle and colored catheter artifacts is shown in (d). It is important to note that while catheters maintain the grid pattern of the template close to the patient’s perineum, they lose the pattern due to bending and crossing as they get closer to the uterus. This complicates the segmentation problem, and is addressed by our method which starts from the distal end of each catheter and tracks it to the base of the template.

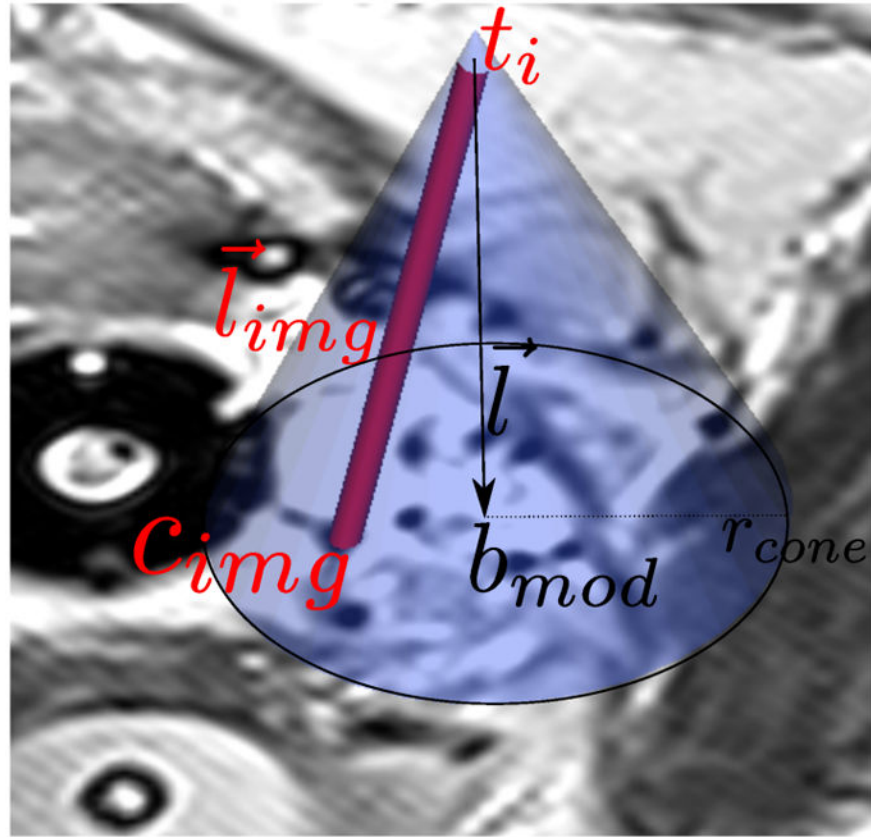
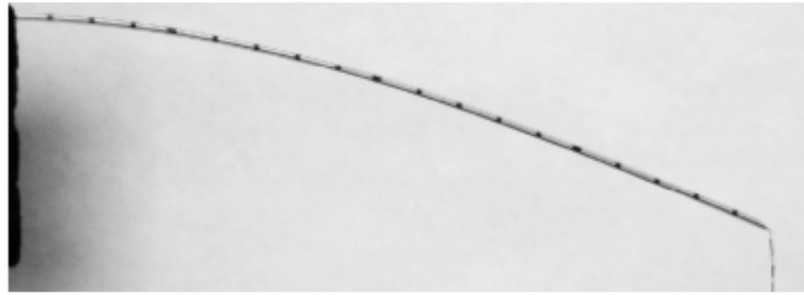
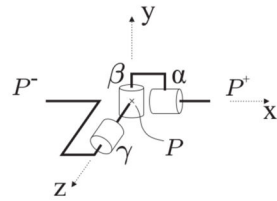


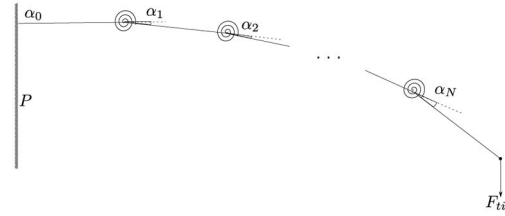
Figure 3. Search cone initialized with t_i as the tip and point c_{img} found by minimization of the line integral described in Eq. 1. r_{cone} is the radius of the cone and is a parameter of the search algorithm.



(a)



(b)



(c)

Figure 4.

(a) Example of a deflected catheter with a weight at the catheter tip. The left end is fixed in a grid (Goksel et al., 2009). (b) Three deflection angles α , β and γ describe the bending around the axes of a local joint coordinate system (Goksel et al., 2009). (c) A one degree of freedom fixed base catheter configuration for one angle α and a force acting on the catheter tip that propagates through the rods and springs (Dehghan et al., 2006).

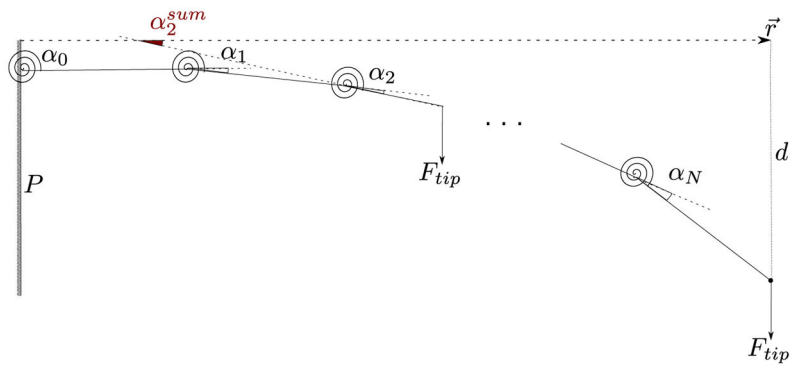


Figure 5.

In *forward calculation* the fixed end of the catheter is provided as initialization. P is the base insertion plane, \vec{r} is the geometry of the unbent reference catheter, d is the deflection of the tip from catheter \vec{r} , α_2^{sum} is the angle between the third rod (counting from the base) of the angular spring and \vec{r} , and F_{tip} is a known gravity force acting on the tip.

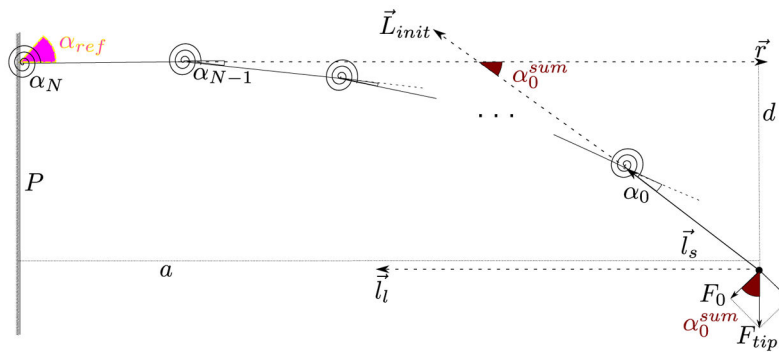
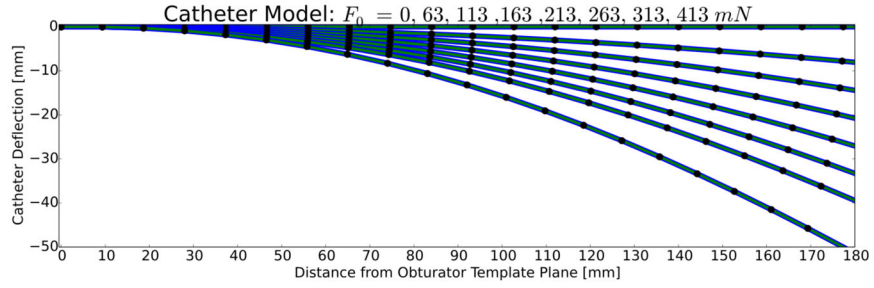
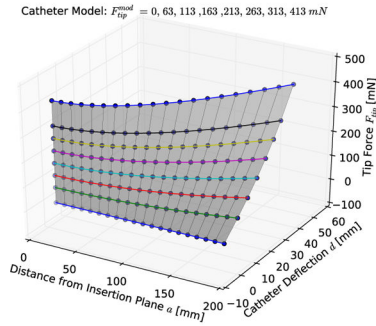


Figure 6.

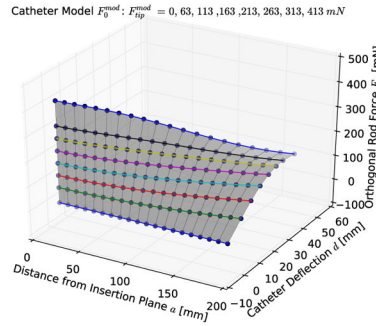
In *backward calculation*, the free end of the catheter is provided as initialization. The distance [mm] from the catheter tip to the base insertion plane P is a ; \vec{r} is the geometry of the unbent catheter; d is the linear deflection of the tip from catheter \vec{r} ; α_0^{sum} is the angle between the first (starting at the tip) rod; and \vec{r} and F_{tip} is a known gravity force acting on the tip. \vec{l}_l and \vec{l}_s are central search cone axes spanning search cones in the image. α_{ref} is the angle from \vec{r} to the scanner system z-axis.



(a)



(b)



(c)

Figure 7. Illustration of simulated continuous catheter models (grey surface) and individual catheter instances (horizontal lines of same color, e.g., red: $F_{tip} = 113 \text{ mN}$): (a) Consistency of our simulation (Mastmeyer et al., 2015) with (Goksel et al., 2009; Dehghan et al., 2006) [R1.5]. (b) With estimated deflection d [mm] and distance from the base template plane a [mm] we can identify the catheter model parameters. (c) With given d and a we can also estimate F_0 from the model F_0^{mod} and yield parameter estimates for every catheter covered by the model.

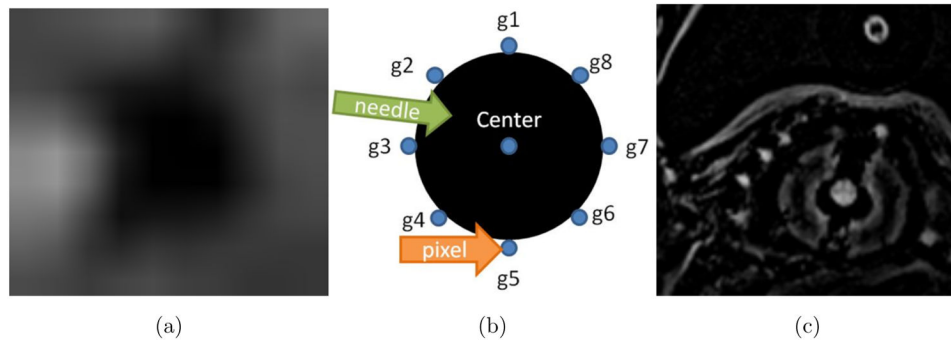


Figure 8.
(a) Catheter image artifact, (b) circular mask matching the characteristics of the artifact and
(c) applied mask to MRI image data.

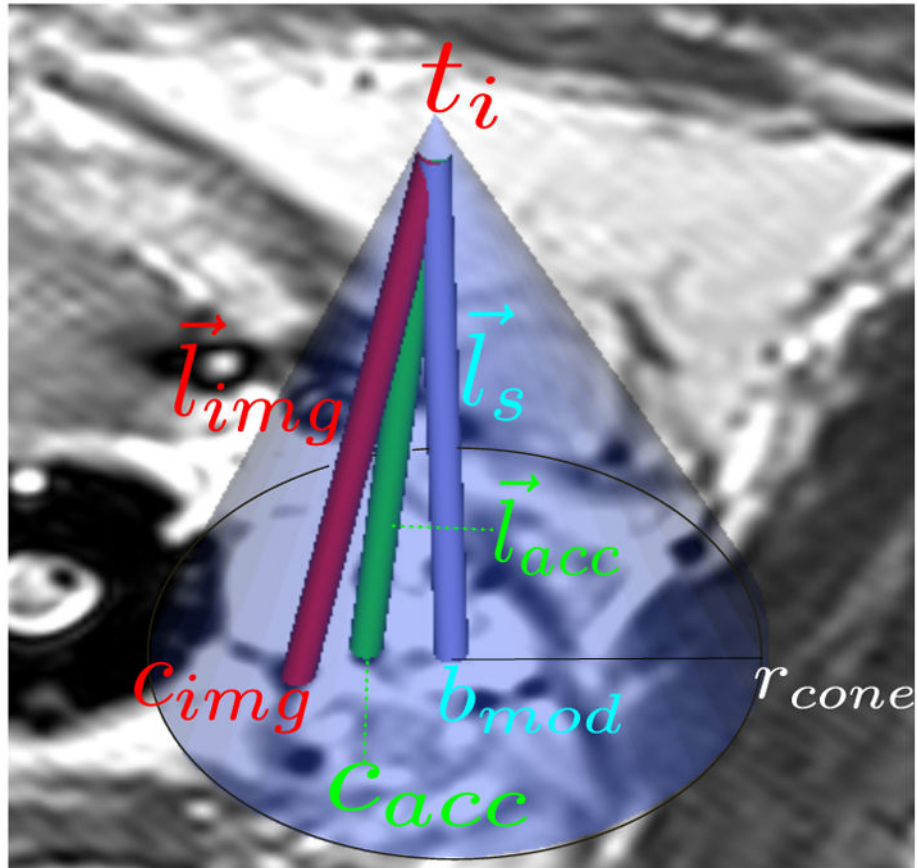


Figure 9. Search cone with c_{img} from Fig. 3. The point b_{mod} is proposed by the angular spring model. c_{acc} is the compromise between them if the distance constraint is violated.

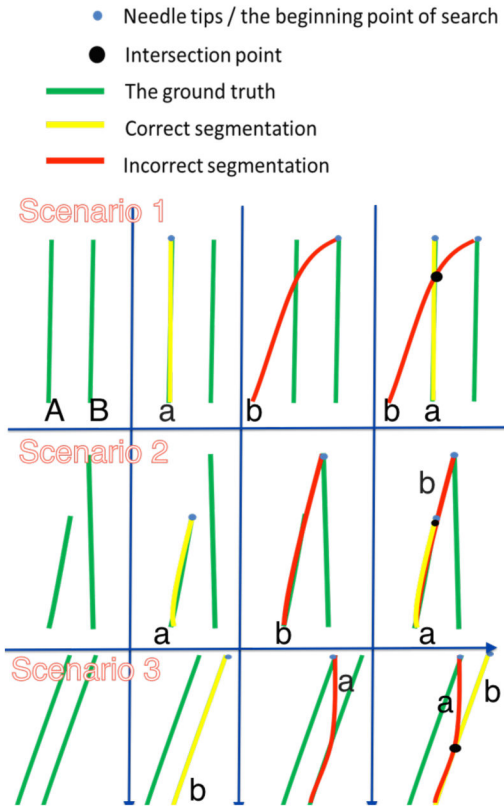


Figure 10.

Three scenarios to illustrate how two catheters close to each other can lead to one being segmented erroneously. Scenario 1: (left) catheters A and B are close to each other and roughly parallel; (middle left) catheter A is segmented correctly, the result is labeled "a" and colored yellow; (middle right) catheter B segmentation, labeled "b" and colored red, starts off with a good tip location but gets pulled towards the artifact of catheter A; (right) Both segmented catheters together. Scenario 2: (left) catheters A and B slope towards one another, and A does not reach as deeply into the patient as B does; (right) Both segmented catheters together, "a" is correct and "b" is wrong. Scenario 3: (left) this is a combination of problems from the first two scenarios; (middle left) catheter B is segmented correctly, the result is labeled "b" and colored yellow; (right) Both segmented catheters together. "b" is correct and "a" is wrong.

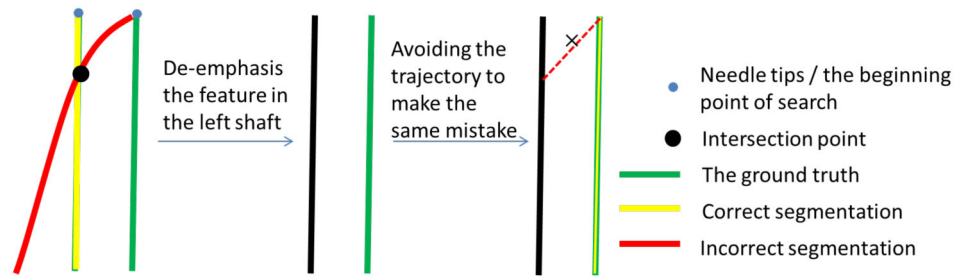


Figure 11.

Modify Step: De-emphasizing, in the context of dark catheter artifacts means artificially creating a bright artifact along a supposedly incorrect trajectory.

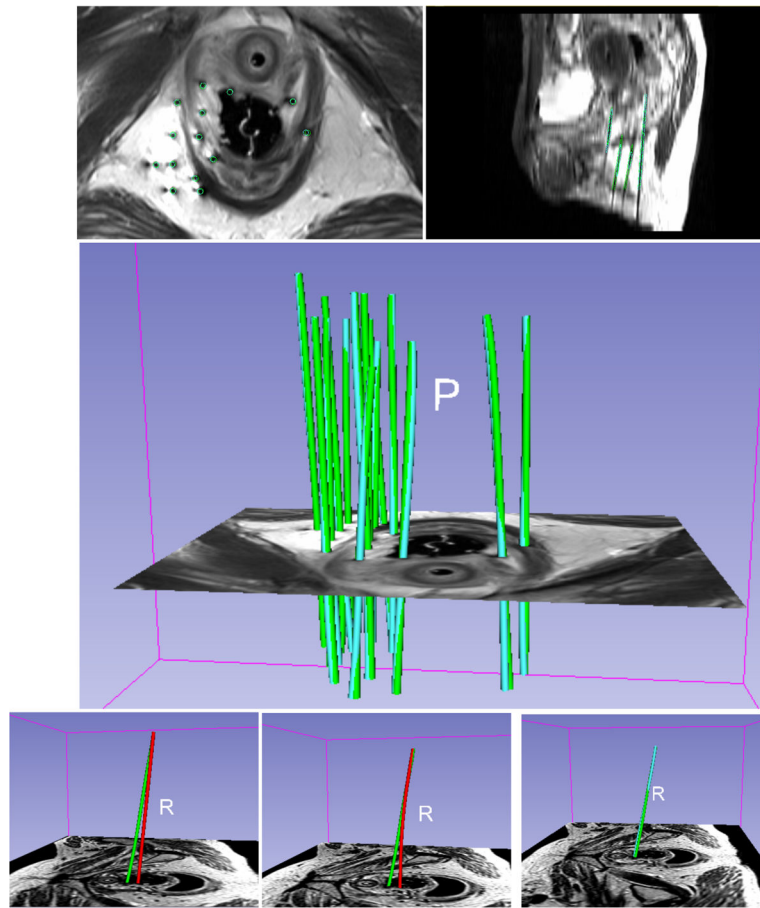


Figure 12.

Two case examples. Upper row: (left) axial view, (right) sagittal view. Middle row: 3D rendering with cross-section. Segmentations of catheters (light blue) from a T2-weighted MR scan of a GYN brachytherapy patient vs. manual segmentations (green). Lower row: A selected difficult catheter: (left) Outlier segmentation results if the method ignores image features (red); (middle) It also fails if the model is ignored (red); (right) In the success case, the hybrid method mode is used (light blue).

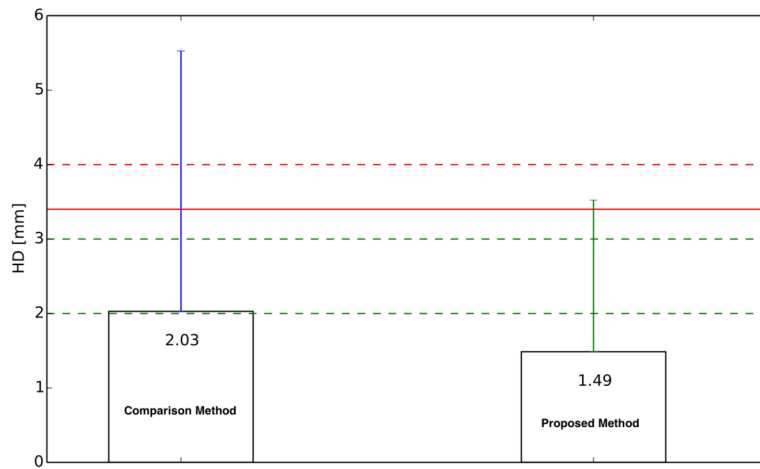
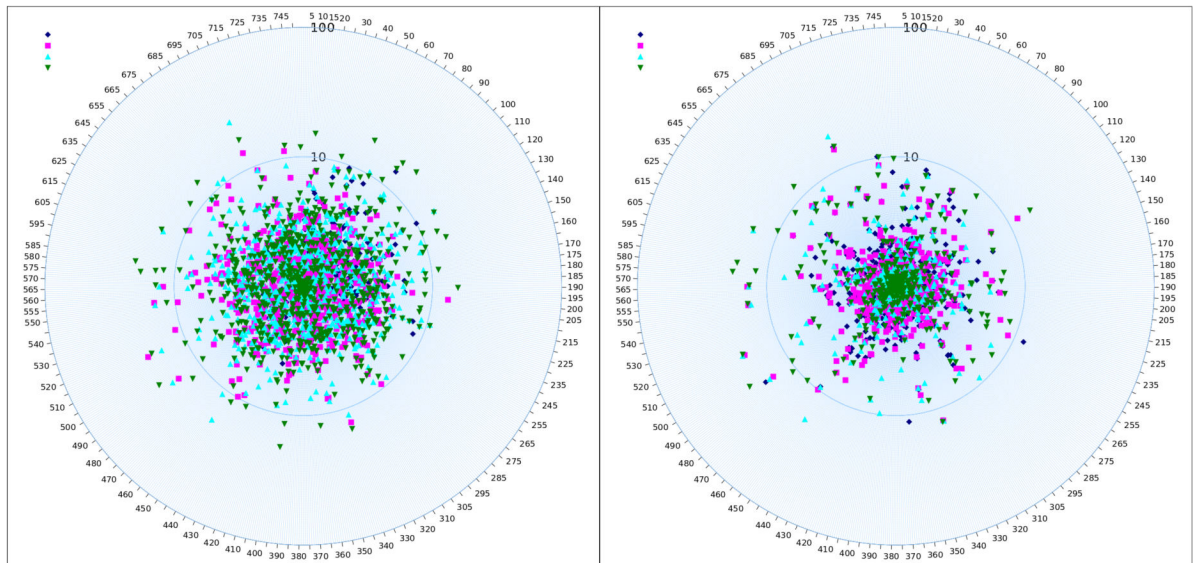


Figure 13. Accuracy Comparison Boxplots of the two methods with 760 catheters: Barcharts, mean and standard deviations (error bars) of Hausdorff distances (HD) [mm] (HD>2 mm, lowest green line; HD>3 mm, middle green line; HD>3.4 mm, solid red line; HD>4 mm, top red line).



(a) Comparison method (Pernelle et al., 2013)

(b) Proposed method

Figure 14.

Hausdorff Distance darts charts for 760 catheters on radial lines displaying the errors on a logarithmic scale (outer ring: 100 mm, middle ring: 10 mm) from four simulated user tries (colored points): (a) The maximum deviation is with the method compared to (Pernelle et al., 2013). (b) Our new method moves a lot of outliers towards the lower errors, which is good. These figures indicate how our new method (b) enhances the precision of catheter segmentation.

Accuracy results for 760 catheters measured as the Hausdorff Distance (HD) between the segmentation method and reference segmentations. 93% of catheters are segmented within a clinically acceptable accuracy of $HD_{crit} = 3.4$ mm [R3.12].

Table 1

HD 2 mm	HD 3 mm	HD 3.4 mm	HD 4 mm	\overline{HD}	\widetilde{HD}
657 (86%)	702 (92%)	709 (93%)	716 [R2.2] (94%)	1.49 mm	2.04 mm

Precision results with 760 catheters and four user tries. The more conservative % CV_{RMS} is 20% higher than its non-RMS counterpart $\overline{\%CV}$. The same holds for the estimated deviations in mm.

Table 2

\overline{HD}	$\overline{\%CV}$	$\tilde{D}_{\%CV}$	$\%CV_{RMS}$	$\tilde{D}_{CV_{RMS}}$	$\overline{HD} + 3 \cdot \tilde{D}_{CV_{RMS}}$
1.57 mm	15.84 %	0.25 mm	18.66 %	0.29 mm	2.44 mm

Accuracy comparison results with 760 catheters: The first four columns show the number of catheters exceeding a Hausdorff Distance threshold (and the corresponding percentage). The top row is the proposed method and the bottom row is the comparison method (Pernelle et al., 2013).

Table 3

Method	HD 2 mm	HD 3 mm	HD 3.4 mm	HD 4 mm	\overline{HD}	\widehat{HD}
Proposed	657 (86%)	702 (92%)	709 (93%)	716 (94%)	1.49 mm	2.04 mm
Comparison(Pernelle et al., 2013)	631 (83%)	658 (87%)	665 (88%)	673 (89%)	2.03 mm	3.50 mm

Precision results with 760 catheters and four user tries. The more conservative % CV_{RMS} is 20–40% higher than its non-RMS counterpart $\overline{\%CV}$. The same holds for the estimated deviations in mm. Significantly lower %CV precision errors were found in proposed method ($p < 0.006$).

Table 4

Method	\overline{HD}	$\overline{\%CV}$	$\tilde{D}_{\%CV}$	$\%CV_{RMS}$	$\tilde{D}_{CV_{RMS}}$	$\overline{HD} + 3 \cdot \tilde{D}_{CV_{RMS}}$
Proposed	1.57 mm	15.84 %	0.25 mm	18.66 %	0.29 mm	2.44 mm
Comparison (Pernelle et al., 2013)	2.37 mm	23.08 %	0.55 mm	27.89 %	0.66 mm	4.35 mm